Design of Load-Bearing Materials for Isolation of Low-Frequency Waterborne Sound

Binghao Zhao, Dongwei Wang,[*] Pingzhang Zhou, Xiaoning Liu, and Gengkai Hu[†]
School of Aerospace Engineering, Beijing Institute of Technology, Beijing 100081, China

(Received 17 September 2021; revised 8 January 2022; accepted 24 February 2022; published 25 March 2022)

Materials with extremely low impedance like air can insulate efficiently waterborne sound, particularly at low frequency, however the poor resistance to load hinders further their applications. This work demonstrates that the elastic anisotropy of materials can not only achieve extremely low impedance, but also high enough stiffness for load bearing. A dimensionless quality factor is proposed to characterize integrately the performance on sound insulation and load bearing of anisotropic materials. It is found that this factor has an upper bound of unity and the corresponding conditions are derived for some particular anisotropic materials. By setting the quality factor to be unity as an objective function for microstructure optimization, a methodology based on topological optimization is proposed to design the microstructure of the corresponding materials with optimized integrated performance on waterborne sound insulation and load bearing. The obtained optimized material is validated by numerical simulation and by comparing with other similar waterborne sound insulation materials with low impedance. This study paves the way for designing load-bearing materials with extremely low impedance, and opens a route to control low-frequency underwater waves.

DOI: 10.1103/PhysRevApplied.17.034065

I. INTRODUCTION

Waterborne sound control plays a role in underwater detection and communication. Engineering applications require farther detection distance and deeper penetrating ability, therefore underwater acoustic control is developing towards low frequency [1–8]. Underwater acoustic insulating materials have been widely used in underwater equipment to insulate and control unwanted noises [9–17]. Compared to the limited bandwidth band gaps, induced by Bragg scattering or local resonance in phononic metamaterials [18–22], the method of impedance mismatch between material and liquid medium is still the most feasible to achieve broadband sound insulation. Common solids, such as metals or polymers, have impedance being 3 or 4 orders larger than that of air but only several tens larger than that of water. Therefore, a solid plate with small thickness can efficiently stop airborne sound but can hardly block waterborne sound, especially at low frequencies. As wave frequency decreases, the thickness of the plate needs to be further increased. This is not conducive to the industry's demand for lightweight. So, the high-impedance solid materials can no longer satisfy the current demand for underwater low-frequency sound insulation.

Contrary to the high-impedance approach, using low-impedance material can also realize an efficient water sound insulation. Air is one such example with impedance being about 3 orders of magnitude smaller than water [23–26]. In fact, air is one of the most efficient mediums for blocking water sound, e.g., the thickness of a steel plate is required to be greater than 0.5 m in order to achieve 10-dB energy attenuation of the underwater sound at 500 Hz, but only 0.0002 m if with air. However, the traditional low-impedance materials, such as air, generally suffer from low stiffness, which cannot meet the pressure-bearing requirement for practical deepwater engineering.

Ideal underwater sound-insulation materials are required to encompass low relative impedance and high enough modulus simultaneously. For traditional isotropic materials, these two properties are positively correlated with each other, i.e., the impedance increases as the modulus increases. Due to this contradiction between large modulus and low impedance, the traditional isotropic materials are proved to be inadequate inherently to achieve the goal. Therefore, a design principle for developing underwater metamaterials with both pressure-bearing and sound-insulation properties is necessary. The key guideline of the design is to break the positive correlation between impedance and stiffness, this needs a profound understanding on water sound insulation and pressure-bearing mechanisms.

Diverse artificial structures with nontraditional properties have been widely used in low-frequency acoustic control and they can be easily manufactured using

[*]wangdw@bit.edu.cn
[†]hugeng@bit.edu.cn

current advanced manufacturing technology [10,27–31]. For example, Chen *et al*. proposed artificial anisotropic pentamode materials to regulate waterborne sounds [9,10, 17,32]. An extremely low-impedance honeycomb pentamode metamaterial was designed to achieve strong sound-insulation performance [9]. This work demonstrates that the normal impedance of an orthotropic material is not only related to the sound speed and equivalent density of the material, but also related to the off-axis angle between its material principal axis and incoming wave. The equivalent interface impedance can be expressed as $Z = \rho c g$, where g is an alternative parameter related to anisotropy of the material and off-axis angle. By changing the value of g and the sound speed of the material, the characteristic impedance of the material under normal incidence can be adjusted. It is found that by rotating the principal axis of the material the characteristic impedance and stiffness can be altered greatly [9]. This discovery provides a feasible basis for designing low-impedance and high-stiffness materials. The objective of this work is to propose a general method to design low-impedance waterborne sound-insulating materials with a good pressure-carrying capability.

The paper starts from examining the sound insulation and load-bearing mechanisms. A dimensionless index (quality factor) is proposed to characterize the overall load-bearing and sound-insulation performances of materials. We further find that there is an upper bound of this parameter, and the way that reaches this upper limit is not unique. This paper analyzes in detail how to use a combination of anisotropy, off-axis angle, and adjustment of parameters to make the proposed quality factor reach the limit. Finally, a general methodology based on topological optimization is proposed to design the optimal microstructure enabling us to have both high load-bearing and high sound-insulation performances. This is explained in Sec. III, and followed by some conclusions.

II. THEORETICAL ANALYSIS

A. Proposition of quality factor Q

To study pressure-bearing and waterborne sound-insulation performances of an anisotropic material, we analyze the acoustic transmission of a plane wave normally incident onto an interface separating water and a solid as shown in Fig. 1.

We first introduce three parameters, the ratio of the material modulus E_s in the incident direction of the sound wave to the bulk modulus K_0 of water $E_x = E_s/K_0$, the relative effective acoustic impedance of the material Z_s normalized by water $Z = Z_s/Z_0$ and the relative effective density of the material ρ_s normalized by water $\rho_{\text{eff}} = \rho_s/\rho_0$. We assume the bulk modulus $K_0 = 2.25$ GPa and acoustic impedance $Z_0 = \rho_0 c_0 = 1.5 \times 10^6$ N s/m^3 for water (the mass density $\rho_0 = 1000$ kg/m^3 and sound speed $c_0 = 1500$ m/s for water). The reflection coefficient R between water and the solid material is $R = |(Z-1)/(Z+1)|$. To integrately investigate the performance of pressure resistance and sound insulation, a dimensionless quality factor Q involving modulus, impedance, and mass density ratios, is defined as

$$Q = E_x\, \rho_{\text{eff}}/Z^2. \tag{1}$$

It can be seen from the definition that high modulus (loading bearing) and low impedance (waterborne sound isolation) lead to high Q. For isotropic materials, Q can be simplified as $Q = E_x\ \rho_{\text{eff}}/Z^2 = 1 - \nu^2$. The proposed quality factor is bounded from upper side by unity in the case of the vanishing Poisson ratio. It is demonstrated later that

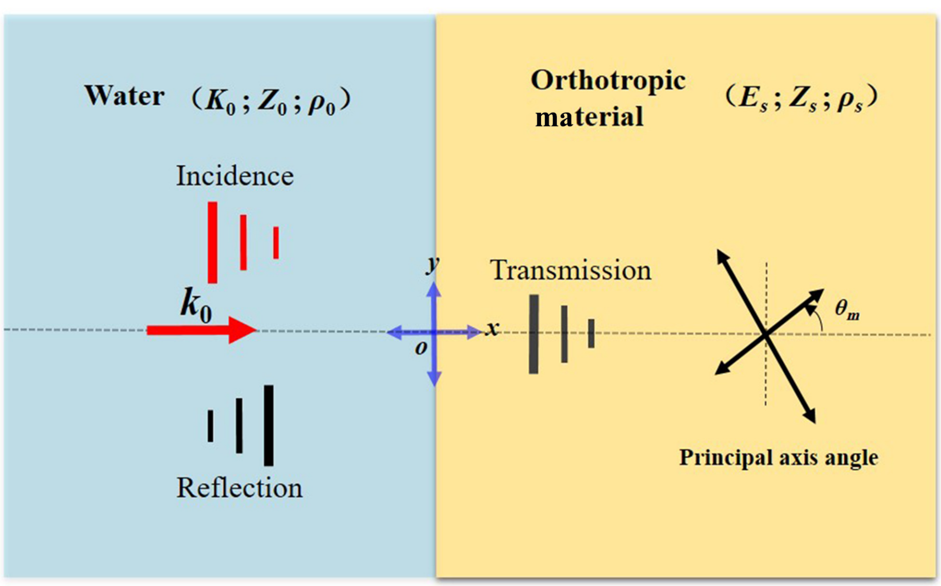

FIG. 1. Acoustic transmission of a plane wave normally incident onto an interface separating water and a solid. The material is supposed to be orthotropic with the principal axis orientated at an angle θ_m with respect to the horizontal direction.

the upper-bound nature for Q still holds for anisotropic materials.

To get the general explicit expression of Q, we primarily study the modulus and impedance of a general two-dimensional orthotropic material. The normalized elastic matrix $\mathbf{C}$ of the material in the principle coordinate system can be expressed as

$$C_0 = \begin{pmatrix} C_{11}^0 & C_{12}^0 & 0 \\ C_{12}^0 & C_{22}^0 & 0 \\ 0 & 0 & C_{66}^0 \end{pmatrix} = \begin{pmatrix} 1 & \sqrt{K\beta} & 0 \\ \sqrt{K\beta} & \beta & 0 \\ 0 & 0 & \gamma \end{pmatrix} C_{11}^0, \tag{2}$$

where C_{11}^0 and βC_{11}^0 denote the normalized modulus of the orthotropic material in x and y directions to the bulk modulus K_0 of water, respectively. The material anisotropy is partially determined by β. K is the product of Poisson's ratio $K = \nu_{21} \times \nu_{12}$, and γC_{11}^0 denotes the normalized shear modulus of the orthotropic material.

The general normalized equivalent elastic matrix $\mathbf{C}$ of the material with a rotation angle of the principal axis θ_m with respect to horizontal direction (wave incident direction) can be derived as

$$\mathbf{C} = \mathbf{N}\mathbf{C}_0\mathbf{N}^T = \begin{pmatrix} C_{11} & C_{12} & C_{16} \\ C_{12} & C_{22} & C_{26} \\ C_{16} & C_{26} & C_{66} \end{pmatrix}, \tag{3}$$

where $\mathbf{N}$ denotes the coordinate transformation matrix. The elements of $\mathbf{C}$ and $\mathbf{N}$ are listed in Appendix A. Then, the equivalent compliance matrix $\mathbf{M}$ can be expressed as

$$\mathbf{M} = \mathbf{C}^{-1}. \tag{4}$$

The normalized modulus along x-axis direction E_x, which can roughly characterize the load-bearing performance under a hydrostatic pressure, is obtained,

$$E_x = 1/\mathbf{M}(1,1) \tag{5}$$

For the orthotropic material with a normally incident wave, the displacement field in the solid $\mathbf{u} = t_{\mathrm{QL}}\mathbf{u}_{\mathrm{QL}} + t_{\mathrm{QT}}\mathbf{u}_{\mathrm{QT}}$ is a combination of the quasilongitudinal (QL) wave $\mathbf{u}_{\mathrm{QL}} = \{1, v_{\mathrm{QL}}\}\exp(ik_{\mathrm{QL}}x)$ and the quasitransverse (QT) wave $\mathbf{u}_{\mathrm{QT}} = \{1, v_{\mathrm{QT}}\}\exp(ik_{\mathrm{QT}}x)$, where v_{QL} (v_{QT}), k_{QL} (k_{QT}) and t_{QL} (t_{QT}) are the polarization coefficient, wave number and transmittance coefficient for the QL (QT) wave, respectively [9]. The displacement can be obtained by solving the dynamic elasticity equation $-\omega^2\rho_s\mathbf{u} = \nabla\cdot\boldsymbol{\sigma}$, where $\boldsymbol{\sigma}$ is the stress tensor.

The total pressure in the incident field is

$$p_1 = p_i \exp(ik_0x) + p_r \exp(-ik_0x), \tag{6}$$

where p_i and p_r, respectively, denote the amplitudes of the incident and reflected waves, k_0 is the wave number in water. Considering the continuous conditions for the normal displacement and the surface traction at the water-solid interface, the expression of the normalized relative acoustic impedance Z of the anisotropic solid materials is derived,

$$Z = \sqrt{\frac{C_{11}^0\rho_{eff}\,(2\Phi_2+\Delta)(2\Phi_2-\Delta)}{4}} \times \frac{[(2\Phi_1+\Delta)^2+\Phi_3^2]}{(2\Phi_1+\Delta)^2\sqrt{(2\Phi_2-\Delta)}+\Phi_3^2\sqrt{(2\Phi_2+\Delta)}}, \tag{7}$$

where $\Phi_1 = (C_{11} - C_{66})/C_{11}^0$; $\Phi_2 = (C_{11} + C_{66})/C_{11}^0$; $\Phi_3 = -4C_{16}/C_{11}^0$, and $\Delta = \sqrt{4\Phi_1^2 + \Phi_3^2}$. The detail expressions of Φ_i and the displacement are given in Appendix B.

Therefore, the quality factor Q, which measures the integrated performance of load-bearing and sound insulation, can be expressed as

$$\mathrm{Q} = \frac{4E_x\left[(2\Phi_1+\Delta)^2\sqrt{(2\Phi_2-\Delta)}+\Phi_3^2\sqrt{(2\Phi_2+\Delta)}\right]^2}{C_{11}^0(2\Phi_2+\Delta)(2\Phi_2-\Delta)[(2\Phi_1+\Delta)^2+\Phi_3^2]^2}. \tag{8}$$

B. Upper bound on the quality factor Q

In order to design materials with low impedance and large modulus, the quality factor Q is expected to be as large as possible. However, it is found that this index has an upper bound. We further examine the conditions for the Q value to reach the upper bound for different kinds of materials.

For isotropic materials, the variables in Eqs. (2) and (6) are simplified as $\beta = 1$, $K = \nu^2$, $\gamma = (1 - \sqrt{K})/2$, and $\Delta = 2\Phi_1$. Subsequently, the quality factor Q is reduced to

$$Q = \frac{E_x\rho_{\mathrm{eff}}}{Z^2} = 1 - K. \tag{9}$$

The maximum value of Q for an isotropic material is found to be 1 when $K = 0$. The isotropic materials with the zero Poisson ratio possess the smallest impedance and the longitudinal wave speed. This is due to the fact that the longitudinal wave speed in isotropic materials is not only influenced by the bulk strain of the materials, but also related to the shear strain. The zero Poisson ratio of the materials causes the Lamé constant $\lambda = 0$, resulting in a vanishing contribution of the dilatational strain. Therefore, the smallest longitudinal wave speed makes the Q value reach the maximum in such situation.

For the case of standard orthotropic materials without axis rotation, i.e., $\theta_m = 0°$ or $90°$, the shear modulus coefficient Φ_3 is always equal to 0 and $\Delta = \pm 2\Phi_1$, which takes the same sign as $1-\gamma$. If $\gamma \le 1$, the expression of the quality factor Q is simplified as Eq. (9). Otherwise when $\gamma > 1$, the Q is simplified as

$$Q = \frac{E_x \rho_{\mathrm{eff}}}{Z^2} = \frac{C_{11}^0 (1-K)}{C_{66}^0}. \tag{10}$$

It is easy to find that in both cases, when $K = 0$, the maximum value of Q of the standard orthotropic materials is reached to be 1.

For the case of general anisotropic materials with arbitrary rotation angle, the upper bound of Q expressed in Eq. (8) can be obtained by parametric and numerical analysis. Figure 2(a) shows the cloud image of the Q value in the ranges $\rho_{\mathrm{eff}} = 1$, $0 \le \beta \le 1.0$, $0 \le \gamma \le 5$ using the parameter scanning method. The values of Q no more than1 in the figure suggest that the quality factor is bounded from upside by 1 whether the materials are isotropic or anisotropic. The dark red color in the figure implies the Q values are close to the upper bound. Unlike the quality factor Q of isotropic or standard orthotropic materials reaching the upper bound only when $K = 0$, the Q value of general anisotropic materials may reach or approach the upper bound in different ways, each corresponding to one set of material parameters. Figures 2(b)–2(e) show the cloud images of the Q value with specific β and γ. Figure 2(b) ($\beta = 0.1$, $\gamma = 0.5$) illustrates that additional maximum of Q occur when $K \neq 0$ (e.g., $K = 0.1$, $\theta_m = 29°$). These conclusions can also be found in Figs. 2(c) and 2(d). Figure 2(e) also shows that for some specific modulus, the Q value can not reach 1 with any K or θ_m.

In order to further investigate the influence of anisotropic material parameters on Q, the variation curves of the normalized effective modulus E_x, the square normalized impedance Z^2, and the quality factor Q as a function of θ_m with different K, β, γ are plotted in Figs. 3(a*i*), 3(b*i*) and 3(c*i*), respectively. Figure 3(a2) shows that the achievable minimum impedance is mainly determined by K. As K varies from 0 to 1, the peaks of E_x and Q curves with small θ_m become narrow and horizontally move to the medium principle angle, while the peak of Q with large θ_m drops sharply, as shown in Figs. 3(a1) and 3(a3). Comparing the changing ranges of E_x and Z^2, the peak of Q with small θ_m is primarily determined by the modulus while the one with large θ_m is mainly controlled by the impedance.

Contrary to K, the increase of β makes the peak of the E_s curve rise and broaden [Fig. 3(b1)] and the two peaks of Q combine together [Fig. 3(b3)]. In addition, a small value of β causes obvious negative correlation between the material impedance and modulus [$\beta = 0.001$, $\theta_m = 0$–$8°$ in Figs. 3(b1) and 3(b2)]. This phenomenon is due to the strong anisotropy, which cannot occur in traditional isotropic materials. Hence the anisotropy properties of the material plays a key role in our underwater sound-insulation design.

The dimensionless shear parameter γ determines the range of θ_m available for small impedance. When γ gradually increases from 0 to 5, Figs. 3(c1) and 3(c2), respectively, show that the range of small modulus and impedance gradually decreases. Meanwhile, as shown in Fig. 3(c3), with the increase of γ, the peak value of the quality factor Q gradually increases from about 0.5 to the upper limit value 1 in the beginning, and then gradually decreases. Therefore, the parameter γ is a key factor affecting the peak value of the parameter Q. The above

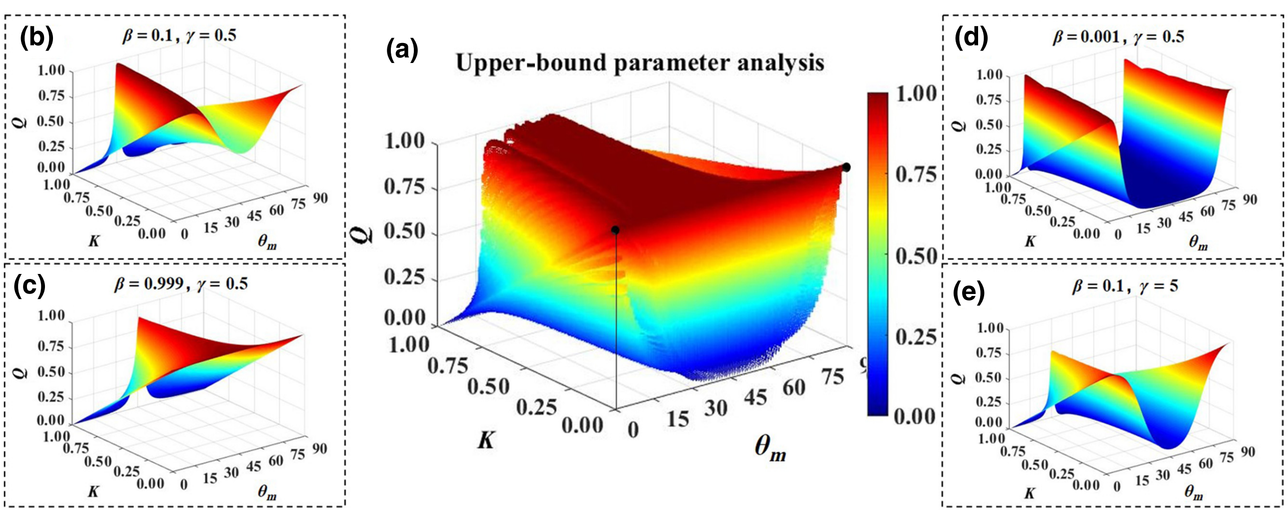

FIG. 2. Parametric analysis of the quality factor Q value versus K and θ_m. (a) $\rho_{\mathrm{eff}} = 1$, $0 \le \beta \le 1.0$, $0 \le \gamma \le 5$. (b) $\beta = 0.1$, $\gamma = 0.5$. (c) $\beta = 0.999$, $\gamma = 0.5$. (d) $\beta = 0.001$, $\gamma = 0.5$. (e) $\beta = 0.1$, $\gamma = 5$.

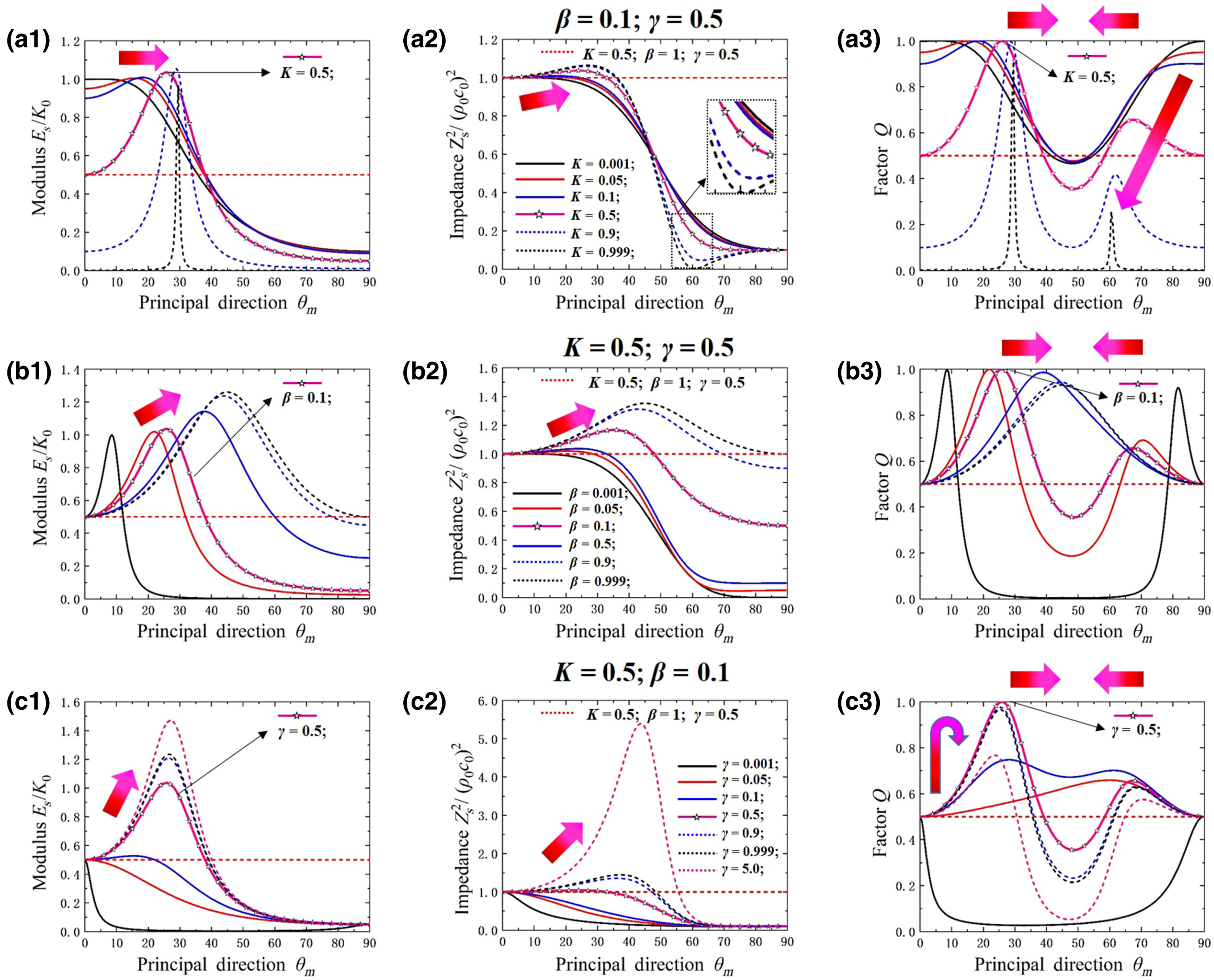

FIG. 3. Influences of (a) K, (b) anisotropy β, and (c) shear parameter γ on normalized effective modulus, square normalized impedance and quality factor of anisotropic materials versus the principal axis angle θ_m.

findings may provide ideas for the design of materials with high load-bearing capacity and high waterborne sound insulation.

C. Phase diagram according to the quality factor Q

We further sort out a phase diagram according to the proposed quality factor for different materials (covering metals, polymers, gases, and common lattice materials, etc.). The quality factor Q as a function of the impedance are depicted in Fig. 4 for different classes of materials.

The metallic materials, concentrated on the upper right corner in the phase diagram surrounded by the black dotted curve, have high impedance and relatively large modulus while the air in the red area over the bottom left corner has the lowest impedance and modulus. Porous foam materials in the area surrounded by the white dotted line can have very low impedance by adjusting different porosity and matrix materials, but the Q value of traditional foam materials without special design cannot reach the upper bound. Among versatile natural isotropic materials, only the quality factor Q of the materials with the zero Poission ratio reaches the upper bound. The anisotropic materials with density $\rho_{\mathrm{eff}} = 0.025$ and $C_{11}^0 = 0.1\ K_0$ cover a wide range in the purple dashed curve. Although the Q value of both isotropic materials with $K = 0$ and some specific anisotropic materials can be close to 1 with the same density, the anisotropic materials possess tremendous potential and designability of low impedance, which is more suitable in underwater engineering design. The targeted materials are expected to locate in the crimson area enclosed by the white solid line (see the insert figure, obj material), where the Q value of the material is close to the upper bound and the effective impedance is small but the

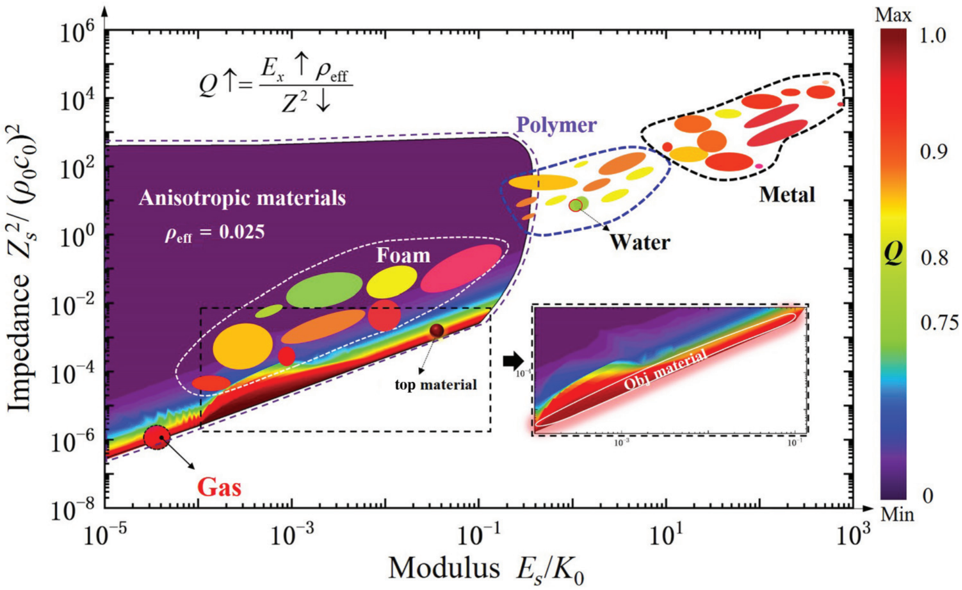

FIG. 4. Ashby diagram: the quality factor Q, the normalized modulus E_x, and the normalized square impedance Z^2 of different classes of materials.

modulus is relatively high. The dark red circular solid area (top material) in Fig. 4 is the topologically optimized lattice in the subsequent chapter that the quality factor Q of the material is close to the upper bound.

So far, we propose a design method based on the anisotropy and the angle of material principal axis to realize low-impedance and high-modulus materials that meet or approach the upper bound of the quality factor Q. In the next section, we propose a general methodology based on topological optimization to design the lattice material that meet the required Q.

III. MICROSTRUCTURAL DESIGN AND NUMERICAL SIMULATION

A. Microstructural design

Based on the previous results on the quality factor Q, we carry out the design of a low-impedance and high-modulus material by the method of topology optimization.

As shown in Fig. 5, the flowchart of the microstructure design can be divided into two parts. In the first part [Fig. 5(a)] a parametric optimization is carried out to find the effective elastic matrix that meets the target conditions and requirements. The second part [Fig. 5(b)] takes advantage of the topology optimization method to find the layout of the microstructure according to the required effective elastic matrix determined in the first part.

The insulating material lattice to be designed is supposed to roughly support a hydrostatic pressure of 1 MPa in the wave incident direction with less than 2% deformation and to block a low-frequency waterborne sound energy with 20-dB energy attenuation. Once the target conditions of the sound-insulation and load-bearing capability are determined, the required Young's modulus and impedance values E_t and Z_t can be obtained as

$$E_t = \sigma/\varepsilon K_0 = 0.089, \quad Z_t = (1-R)/(1+R) = 0.052\,63. \tag{11}$$

The materials with $Z < Z_t$ and $E_x > E_t$ can therefore meet the target. The required equivalent density ρ_{eff} can be easily derived using the integrated optimized condition $Q = 1$.

$$\rho_{\text{eff}} = Q_{\max} Z_t^2/E_t = Z_t^2/E_t. \tag{12}$$

The optimization results of the normalized material parameters are obtained as $C_{11}^0 = 0.0227$, $K = 0.0221$, $\beta = 0.2158$, $\theta_m = 34°$, $\gamma = 0.4405$ by using the parametric optimization method [Fig. 5(a)]. The corresponding Q value is close to 1 and the target effective elasticity parameters of the lattice are, respectively, $C_{11}^0 = 0.0227$, $C_{22}^0 = 0.0049$, $C_{12}^0 = 0.0104$, and $C_{66}^0 = 0.01$, and the effective density is $\rho_{\text{eff}} = 0.0292$. The material lattice with these effective elastic parameters possesses extremely low impedance and high modulus.

After getting the effective elastic parameters, in the second part, we apply the density method [Fig. 5(b)], which is the most popular topology optimization method nowadays, to carry out the layout design of the microstructure. The details of the density method are shown in Appendix C.

According to the numerical homogenization method, in total six kinds of prescribed strain fields are needed to

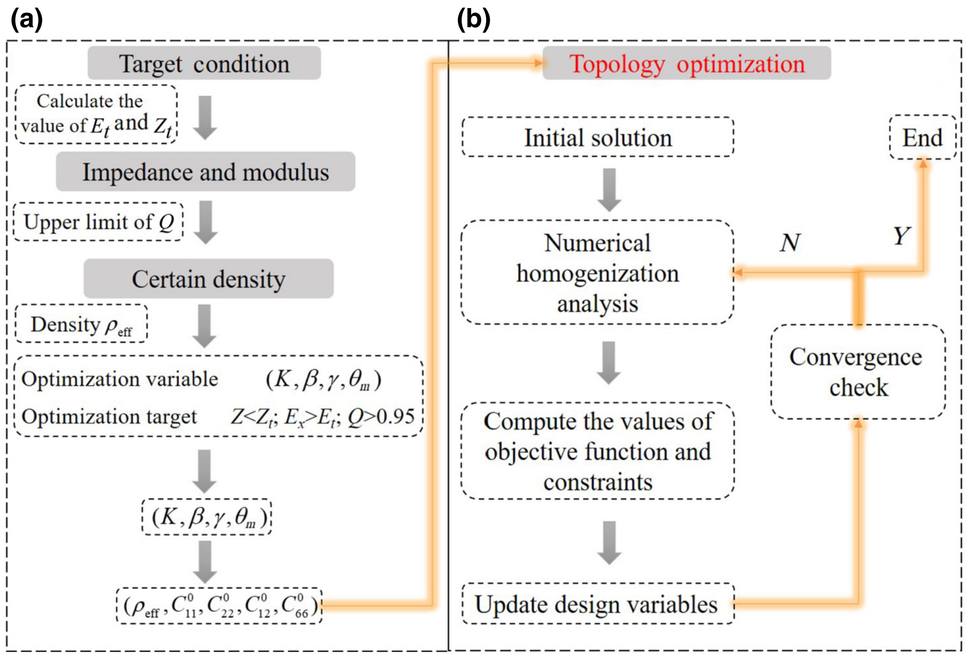

FIG. 5. Material microstructure design logic diagram. Process diagram of (a) parametric optimization to find the material effective elastic matrix and (b) topology optimization method.

uniquely determine the two-dimensional elastic matrix:

$$\begin{aligned}
C_{11} &= \frac{2}{V}\Pi_{[1,0,0]},\\
C_{22} &= \frac{2}{V}\Pi_{[0,1,0]},\\
C_{66} &= \frac{2}{V}\Pi_{[0,0,1]},\\
C_{12} &= \frac{1}{V}\Pi_{[1,1,0]} - \frac{1}{2}(C_{11}+C_{22}),\\
C_{16} &= \frac{1}{V}\Pi_{[0,1,1]} - \frac{1}{2}(C_{11}+C_{66}),\\
C_{26} &= \frac{1}{V}\Pi_{[0,1,1]} - \frac{1}{2}(C_{22}+C_{66}),
\end{aligned} \tag{13}$$

where $\Pi_{[1,0,0]}$ is the strain energy of the unit cell under prescribed strain field $\bar{\boldsymbol{\varepsilon}} = \begin{bmatrix}1 & 0\\ 0 & 0\end{bmatrix}$, the other symbols can be understood in a similar manner.

The objective is to find the microstructure whose effective moduli get close to the ones defined in the previous section, so the mathematical model of the optimization problem can be written as

$$\begin{array}{ll}
\text{Find} & \xi_1,\xi_2,\ldots,\xi_{N_{\rm ele}}\\
\min & (C_{11}-C_{11}^0)^2+(C_{12}-C_{12}^0)^2+(C_{22}-C_{22}^0)^2\\
 & \quad +(C_{66}-C_{66}^0)^2\\
\text{such that} & \begin{cases}\tilde{\mathbf{K}}\tilde{\mathbf{U}}=\tilde{\mathbf{F}},\\ \xi_i\in[0,1]\end{cases}
\end{array} \tag{14}$$

where $\tilde{\mathbf{K}}\tilde{\mathbf{U}}=\tilde{\mathbf{F}}$ is the state equation [Eq. (C8) in Appendix C] of the unit cell under periodic boundary condition.

The mathematical problem Eq. (14) is solved using gradient-based numerical optimization algorithm. More specifically, we use the interior-point algorithm to solve it, Eq. (14). In the interior-point algorithm, the sensitivity information of the objective function and constraint are needed in order to update the design variable in an efficient manner. For a detailed derivation of the sensitivity information, we recommend the readers to turn to Ref. [33].

Finally, the material lattice that satisfies the objective function as shown in Fig. 6(a) can be obtained by the above-mentioned optimization framework. The optimized anisotropic lattice is characterized by three parameters: the square lattice length $L=10$ mm, the dimensionless beam thickness $T/L=0.004$, and the topology angle $\varphi=60°$. All the beams are assumed to be aluminum with mass density $\rho_{\rm Al}=2700$ kg/m^3, Young's modulus $E_{\rm Al}=69$ GPa, and Poisson's ratio $\nu_{\rm Al}=0.33$.

Moreover, the characteristic impedance and Young's modulus of the topologically optimized designed lattice with varying θ_m are depicted in Fig. 6(b). Obviously, the trend of impedance and modulus are different, even opposite, in some range of the principal direction. This means that rotating the principle axis of the optimized anisotropic materials can resolve the contradiction that high modulus and low impedance cannot be designed simultaneously. Clearly, the peak of the quality factor Q at $\theta_m=34°$ corresponds to the targeted values of modulus and impedance as shown in Fig. 6(b) by the green dotted-dashed lines.

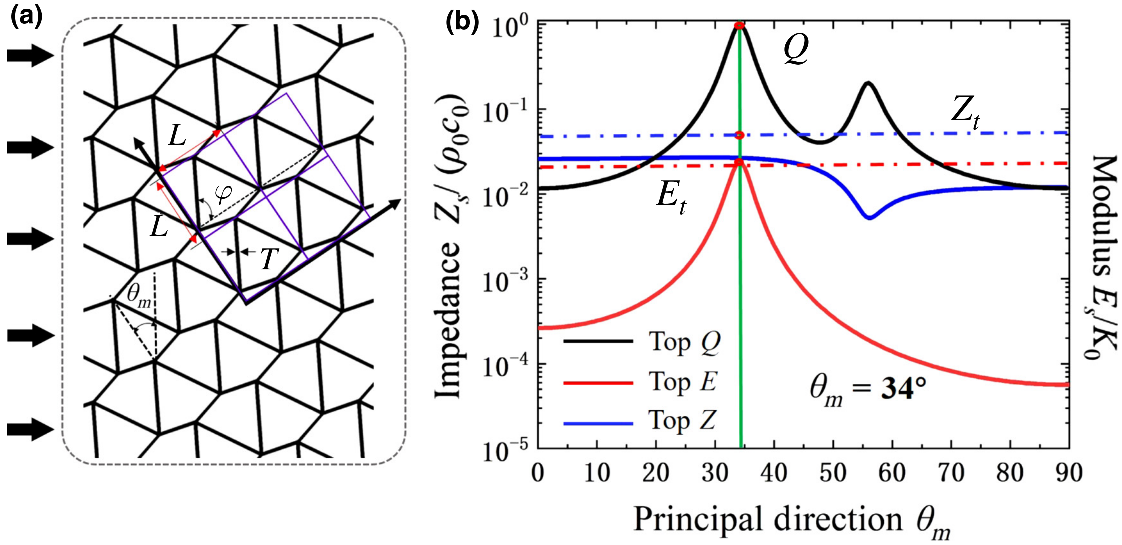

FIG. 6. (a) Topological optimized lattice with lattice vector length L, the dimensionless beam thickness T/L, and the topology angle φ; (b) curves of the impedance, modulus, and the quality factor Q of the topologically optimized designed lattice versus the angle of the principal axis.

B. Numerical validation on sound-insulation property

The simulations are performed using the coupled acoustic-solid module in COMSOL Multiphysics to validate the designed material lattice. Voids in the structures are filled with air ($\rho_{\mathrm{air}} = 1.29$ kg/m^3, $c_{\mathrm{air}} = 343$ m/s), and the background region is occupied by water. The plate thickness is $d = 30$ mm. The frequency range of interest is $0.05\ \mathrm{kHz} \le f \le 3.0$ kHz, or equivalently $16.7\ d \le \lambda \le 1000\ d$. In order to demonstrate the performance, we compare the impedance and modulus characteristics of the topological optimized lattice (top), the isotropic (iso), and anisotropic honeycomb (hon) lattices with equal effective impedance. The HON has been proved to hold extremely excellent sound-insulation property [9].

The honeycomb lattice is characterized by three dimensionless parameters, i.e., the length ratio h/l, the dimensionless beam thickness t/l, and the topology angle ξ, where l and h are, respectively, the short and long side lengths of honeycomb lattice and t donates the thickness of beam. The lattice is isotropic when $h = l$ and $\xi = 60°$, otherwise becomes anisotropic. The normalized effective elasticity parameters of the anisotropic honeycomb lattice ($\xi = 74°$, $h/l = 0.25$, and $t/l = 0.03$) are $C_{11}^0 = 0.0351$, $C_{22}^0 = 3.22$, $C_{12}^0 = 0.3305$, and $C_{66}^0 = 0.0204$. The normalized effective density$\rho_{\mathrm{eff}} = 0.2255$. The principal axis angle of the anisotropic honeycomb beam lattice is rotated by 22.5° in order to gain the same impedance to the optimized lattice (HON1). The normalized effective elasticity parameters of the isotropic honeycomb lattice ($\xi = 60°$, $h/l = 1$, and $t/l = 0.0041$) are $C_{11}^0 = C_{22}^0 = C_{12}^0 = 0.040$ and $C_{66}^0 = 5 \times 10^{-5}$. The corresponding effective density $\rho_{\mathrm{eff}} = 0.0128$. The impedance, modulus, and the quality factor Q of these three materials are compared using the numerical simulation method as shown in Figs. 7(a)–7(c). Three lattices with equal effective impedance have different modulus. The topologically optimized lattice has the largest modulus and the quality factor Q, while the isotropic honeycomb holds the smallest. The modulus gap can even reach 2 orders of magnitude.

To show the sound-insulation properties of the practical structures, the sound reduction indexes (SRIs) of those lattice panels with 30 mm thickness are illustrated in Fig. 7(d). The SRI is expressed as $-20 \times \log_{10}(A_T/A_I)$, where A_T and A_I represent the amplitudes of the transmitted and incident waves, respectively. It is observed that the optimized and anisotropic honeycomb panel (hon1) performs much better than the top and iso panels in waterborne sound insulation. Since the optimized material significantly increases the load-bearing capacity (13 times larger than that of hon1), it sacrifices a little sound-insulation capacity compared to that of the anisotropic honeycomb lattice. Another anisotropic honeycomb panel with the principal axis angle 45° (hon2) holds approximately the same SRI with the top, while its modulus is just a quarter of that of the top. Therefore, the topologically optimized lattice has the best integrate performance.

Furthermore, to show the sound insulation in a more direct way, the transient response of the topologically optimized lattice plate material as well as an aluminum plate with identical thickness are simulated under the incidence of a Gaussian pulse $\exp\{-[\pi f_c(t - 1.25/f_c)/6]^2\} \times \sin(2\pi f_c t)$, with a central frequency $f_c = 750$ Hz. As shown in Figs. 7(e) and 7(f), the optimized lattices perform much

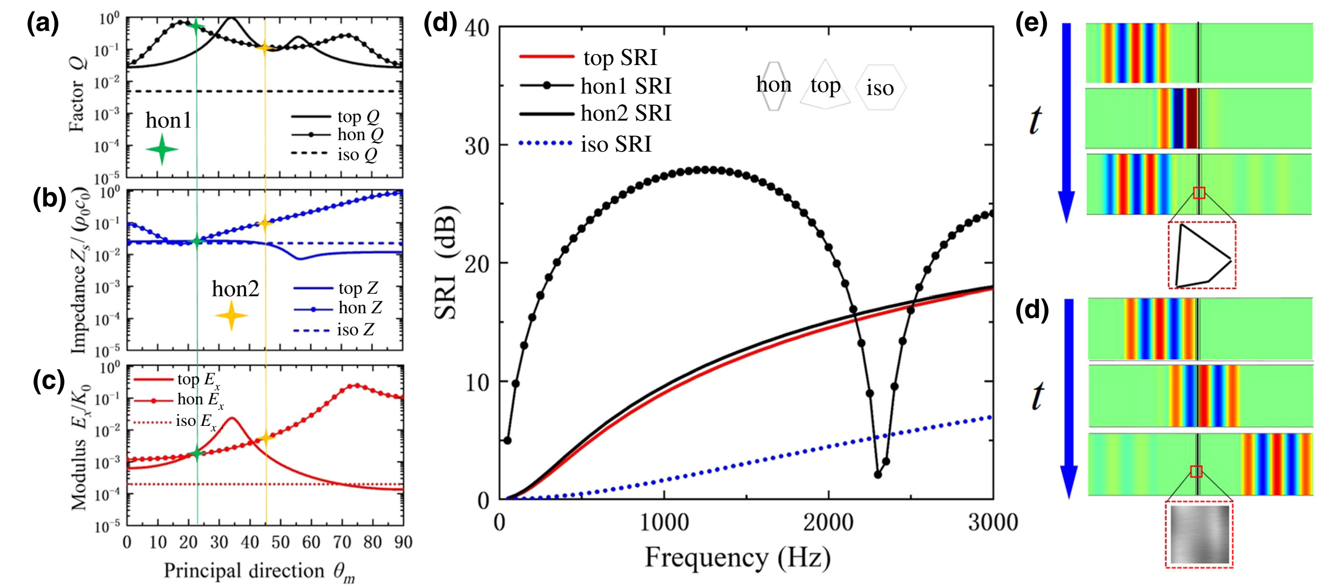

FIG. 7. Numerical analysis of (a) the quality factor Q, (b) the impedance, (c) the modulus of the top, iso, and anisotropic hon lattices with varying principal axis angle of the materials. (d) Comparison between the SRI of top, iso, and hon structures. Simulated pressure fields for transient plane waves incident onto a slab at different time sequences: (e) topologically optimized lattice, (f) pure aluminum.

better than the traditional metal plate in underwater sound insulation.

Our design is based on the normal incidence to simplify the problem, however oblique incident waves can also be treated with the same model by adding the component in y-direction, e.g., $\mathbf{u}_{\mathrm{QL}} = \{1, v_{\mathrm{QL}}\}\exp(ik_{\mathrm{QL}x}x + ik_{\mathrm{QL}y}y)$ where $k_{\mathrm{QL}x}$ and $k_{\mathrm{QL}y}$ are the wave-number components of quasi-longitudinal wave along x and y axis, respectively. The SRI of the optimized lattice panel with obliquely incident waves are plotted in Fig. 8. The results indicate that the optimized structure can also have good performance with oblique incident waves. This is because that the normal wave energy decreases as the incident angle increases, which reduces the transmitted waves accordingly. The approximated tangent incident wave (the incident angle θ_i approaches 90°) causes nearly total reflection.

The SRI curves of the designed material lattice plate with and without pressure versus frequency are illustrated in Fig. 9. Additional SRI curves of the plates of the equivalent homogenized material and aluminum with the same thickness are also plotted for comparison. For waterborne sound insulation based on the low-impedance method,

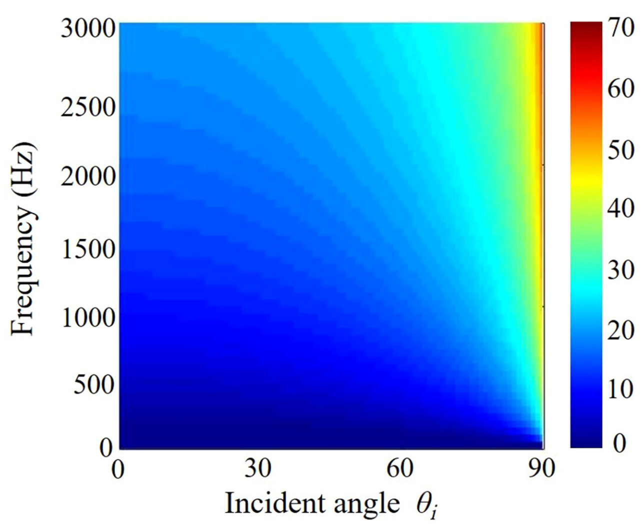

FIG. 8. Calculated SRI of the optimized material lattice versus frequency f and the incident angle θ_i.

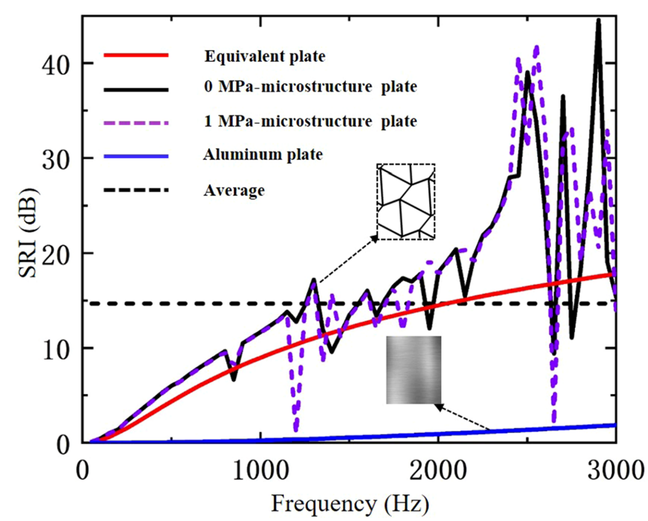

FIG. 9. Numerical simulation SRI for plates composed of the optimized lattice, its homogenized equivalent material and aluminum alloy, respectively.

load-carrying capacity and sound insulation are contradictory to each other. The pressure influences the insulation performance by changing the geometry and stress state of the lattice. For small pressure, the lattice with a relative high modulus has little change in shape under 1 MPa, which leads to small variations in SRI. The average SRI in the range 50 Hz–3.0 kHz is close to 14.78 dB, much larger than the acoustic transparent aluminum alloy plate. The curves of the plate with the optimized microstructure and its equivalent material follow the same trend. The fluctuations of the SRI curve for the lattice plate are mainly attributed to the local resonances and the solid-fluid coupling effects. At 2000 Hz, despite the wavelength being 33.3 times larger than the plate thickness, the subwavelength lattice can block nearly 90% of the incident energy.

It should be noted that the structure under pressure is calculated using a linear solid model because of the small change in shape. For large pressure, the induced large deformations and buckling may deteriorate the microstructure and degrade severely the insulating performance. Moreover, in our design strategy, we have not employed any resonant mechanism and only nondispersive static material property is utilized, so the design material is intrinsically broadband. When the frequency increases to the homogenization limit, our design method is no longer valid. For the dispersive cases, e.g., at high frequencies, the design principle can still be applied, but due to the frequency-dependent material property, this should be done for each frequency and then some target functions should be optimized over interested frequency range.

IV. CONCLUSIONS

To design materials with excellent waterborne sound insulation and load-bearing capacity, we investigate the impedance and modulus of a general anisotropic material. A dimensionless quality factor Q is defined to integrately characterize the underwater sound-insulation and pressure-bearing properties. It is also shown that the quality factor Q is bounded by 1 from upperside, the corresponding attainable conditions of different kinds of materials are studied. The effects of the key material parameters with varying material principle direction on the quality factor Q are analyzed. It is found that Poisson's ratio product K affects the position and the magnitude of peak in the Q curve. Anisotropy β controls the interval of two peaks and the coupling relationship between the modulus and impedance. The shear parameter γ influences the peak value of the quality factor. Based on the results for homogeneous anisotropic materials, we propose a design method to determine the microstructure of the material with the required low impedance and high modulus using the topology optimization method. The optimized materials are shown to possess excellent integrated property. This study provides an additional way to design waterborne sound-insulating materials with load-bearing capacity.

ACKNOWLEDGMENTS

This work is supported by the National Natural Science Foundation of China (Grants No. 11472044, No. 11632003, No. 11802017, No. 11991030, and No. 11991033), and Beijing Science and Technology Commission (Grant No. Z191100004819003). Dr. Yi Chen, from Karlsruher Institut für Technologie, is gratefully acknowledged for his guidance for this article.

APPENDIX A: EXPRESSION OF THE GENERAL EQUIVALENT ELASTIC MATRIX

The general equivalent elastic matrix C of material with rotation angle of principal axis θ_m is expressed as

$$\mathbf{C} = \mathbf{N}\mathbf{C}_0\mathbf{N}^T = \begin{pmatrix} C_{11} & C_{12} & C_{16} \\ C_{12} & C_{22} & C_{26} \\ C_{16} & C_{26} & C_{66} \end{pmatrix}, \tag{A1}$$

where the coordinate transformation matrix N is

$$\mathbf{N} = \begin{bmatrix} \cos^2\theta_m & \sin^2\theta_m & \sin 2\theta_m \\ \sin^2\theta_m & \cos^2\theta_m & -\sin 2\theta_m \\ -\sin\theta_m\cos\theta_m & \sin\theta_m\cos\theta_m & \cos^2\theta_m - \sin^2\theta_m \end{bmatrix}. \tag{A2}$$

The elements of the matrix C are listed below.

$$C_{11} = \frac{1}{8}C_{11}^0\left[3 + 2\sqrt{K\beta} + 3\beta + 4\gamma - 4(-1+\beta)\cos(2\theta_m) + \left(1 - 2\sqrt{K\beta} + \beta - 4\gamma\right)\cos(4\theta_m)\right], \tag{A3}$$

$$C_{12} = \frac{1}{8}C_{11}^0\left[1 + 6\sqrt{K\beta} + \beta - 4\gamma + \left(-1 + 2\sqrt{K\beta} - \beta + 4\gamma\right)\cos(4\theta_m)\right], \tag{A4}$$

$$C_{16} = -\frac{1}{4}C_{11}\left[1 - \beta + \left(1 - 2\sqrt{K\beta} + \beta - 4\gamma\right)\cos(2\theta_m)\right]\sin(2\theta_m), \tag{A5}$$

$$C_{22} = \frac{1}{8}C_{11}\left[3 + 2\sqrt{K\beta} + 3\beta + 4\gamma + 4(-1+\beta)\cos(2\theta_m) + \left(1 - 2\sqrt{K\beta} + \beta - 4\gamma\right)\cos(4\theta_m)\right], \tag{A6}$$

$$C_{26} = \frac{1}{4}C_{11}^0\left[-1+\beta+\left(1-2\sqrt{K\beta}+\beta-4\gamma\right)\cos(2\theta_m)\right]\sin(2\theta_m), \tag{A7}$$

$$C_{66} = \frac{1}{8}C_{11}^0\left[1-2\sqrt{K\beta}+\beta+4\gamma+\left(-1+2\sqrt{K\beta}-\beta+4\gamma\right)\cos(4\theta_m)\right], \tag{A8}$$

$$\mathbf{M} = \mathbf{C}^{-1} = \begin{pmatrix} M_{11} & M_{12} & M_{16} \\ M_{21} & M_{22} & M_{26} \\ M_{61} & M_{62} & M_{66} \end{pmatrix}. \tag{A9}$$

APPENDIX B: EXPRESSION OF THE PARAMETERS IN Eq. (7)

The parameters Φ_1, Φ_2, Φ_3, in Eq. (7) are expressed as

$$\begin{aligned}
\Phi_1 &= (C_{11}-C_{66})/C_{11}^0 = \frac{1}{4}\left[1+2\sqrt{K\beta}+\beta-2(-1+\beta)\cos(2\theta_m)+\left(1-2\sqrt{K\beta}+\beta-4\gamma\right)\cos(4\theta_m)\right], \\
\Phi_2 &= (C_{11}+C_{66})/C_{11}^0 = \frac{1}{4}[2+2\beta+4\gamma+(2-2\beta)\cos(2\theta_m)], \\
\Phi_3 &= -4C_{16}/C_{11}^0 = \left[1-\beta+\left(1-2\sqrt{K\beta}+\beta-4\gamma\right)\cos(2\theta_m)\right]\sin(2\theta_m).
\end{aligned} \tag{B1}$$

The polarization coefficients v_{QL}, v_{QT}, wave numbers k_{QL}, k_{QT} of the displacement field in solid are expressed as

$$v_{\mathrm{QL}} = \frac{-\Phi_3}{2\Phi_1+\sqrt{4\Phi_1^2+\Phi_3^2}},\ v_{\mathrm{QT}} = \frac{-\Phi_3}{2\Phi_1-\sqrt{4\Phi_1^2+\Phi_3^2}},\ k_{\mathrm{QL}} = \frac{\omega}{c_{\mathrm{QL}}},\ k_{\mathrm{QT}} = \frac{\omega}{c_{\mathrm{QT}}}, \tag{B2}$$

where c_{QL} and c_{QT} are the wave velocities, and $\Delta = \sqrt{4\Phi_1^2+\Phi_3^2}$.

$$c_{\mathrm{QL}} = \sqrt{\frac{C_{11}^0\left(4\Phi_2+2\sqrt{4\Phi_1^2+\Phi_3^2}\right)}{8\rho_{\mathrm{eff}}}} = \sqrt{\frac{C_{11}^0(2\Phi_2+\Delta)}{4\rho_{\mathrm{eff}}}}, \tag{B3}$$

$$c_{\mathrm{QT}} = \sqrt{\frac{C_{11}^0\left(4\Phi_2-2\sqrt{4\Phi_1^2+\Phi_3^2}\right)}{8\rho_{\mathrm{eff}}}} = \sqrt{\frac{C_{11}^0(2\Phi_2-\Delta)}{4\rho_{\mathrm{eff}}}}. \tag{B4}$$

APPENDIX C: DETAILS OF THE DENSITY METHOD

In the density method, the design variable $\boldsymbol{\xi}$ is taken to be the fictitious density of each element,

$$\boldsymbol{\xi} = [\xi_1, \xi_2, \xi_3, \ldots, \xi_{N_{\mathrm{ele}}}], \tag{C1}$$

where N_{ele} is the number of elements in the finite-element model, $\xi_i \in [0,1]$ is the fictitious density of ith element.

The stiffness matrix of ith element is related to ith design variable by

$$\mathbf{k}_i = \int_{\Omega_i^e}\mathbf{B}^{\top}\mathbf{D}_i\mathbf{B}d\Omega = \xi_i^3\mathbf{k}_{i0}+(1-\xi_i^3)\mathbf{k}_{i\ \min}, \tag{C2}$$

where $\mathbf{B}$ is the strain-displacement matrix; $\mathbf{k}_{i0}$ and $\mathbf{k}_{i\ \min}$ denotes the stiffness matrix of the element when solid and void materials are completely filled in the unit cell, respectively.

According to the assembly rule in the finite-element method, a global stiffness matrix $\mathbf{K}$ is obtained after the element stiffness matrix is assembled.

$$\mathbf{K} = \sum_{i=1}^{N_{\mathrm{ele}}}\mathbf{k}_i, \tag{C3}$$

where $\mathbf{k}_i$ is the stiffness matrix of ith element.

In order to find the effective moduli of the microstructure, a sequence of simulations needs to be executed by applying the so-called Cauchy-Born boundary condition [33] under different kinds of prescribed strain fields.

Take the square unit cell (shown in Fig. 10) as an example, the Cauchy-Born boundary condition can be

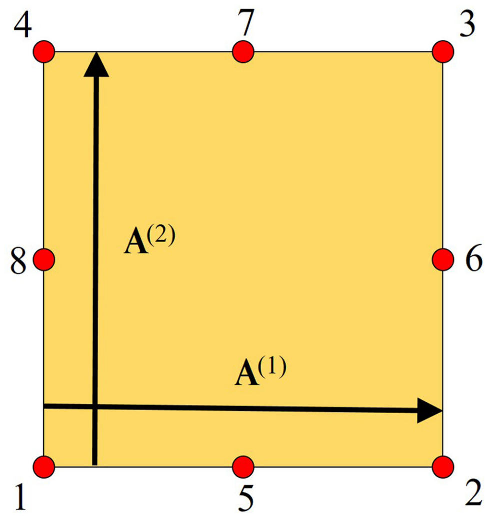

FIG. 10. A unit cell. The exterior boundary nodes are marked with red circles.

given by

$$\begin{aligned}\mathbf{u}_2-\mathbf{u}_1=\mathbf{u}_3-\mathbf{u}_4=\mathbf{u}_6-\mathbf{u}_8=\bar{\boldsymbol{\varepsilon}}\mathbf{A}^{(1)}\\ \mathbf{u}_4-\mathbf{u}_1=\mathbf{u}_3-\mathbf{u}_2=\mathbf{u}_7-\mathbf{u}_5=\bar{\boldsymbol{\varepsilon}}\mathbf{A}^{(2)},\end{aligned}\tag{C4}$$

where $\mathbf{u}_i$ is the displacement vector of ith node; $\bar{\boldsymbol{\varepsilon}}$ is the prescribed strain that is to be exerted on the unit cell; $\mathbf{A}^{(1)}$ and $\mathbf{A}^{(2)}$ are the bond vectors of the periodic unit cells. The Cauchy-Born boundary condition can also be written in a compact matrix form as

$$\mathbf{Pu}=\mathbf{q}.\tag{C5}$$

Note that the matrix $\mathbf{P}$ depends only on the topology of the unit cell, while the vector $\mathbf{q}$ depends on both the topology of the unit cell and the prescribed strain field $\bar{\boldsymbol{\varepsilon}}$.

In order to find the displacement field $\mathbf{u}$ under the Cauchy-Born boundary condition, one should minimize the augmented Lagrangian functional given by

$$\Pi=\frac{1}{2}\mathbf{u}^{\top}\mathbf{Ku}+\lambda^{\top}(\mathbf{Pu}-\mathbf{q}).\tag{C6}$$

Note that in equilibrium state, the augmented Lagrangian functional Π is equal to the potential energy of the unit cell. The extremum condition of the augmented Lagrangian functional Π gives

$$\delta\Pi=0\Rightarrow\begin{cases}\Pi_u=\mathbf{Ku}+\mathbf{P}^{\top}\lambda=\mathbf{0}\\ \Pi_\lambda=\mathbf{Pu}-\mathbf{q}=\mathbf{0}\end{cases}.\tag{C7}$$

The state equations in Eq. (C7) of the unit cell under periodic boundary can be rewritten as

$$\tilde{\mathbf{K}}\tilde{\mathbf{U}}=\tilde{\mathbf{F}},\tag{C8}$$

where

$$\tilde{\mathbf{K}}=\begin{bmatrix}\mathbf{K} & \mathbf{P}^{\top}\\ \mathbf{P} & \mathbf{0}\end{bmatrix},\quad \tilde{\mathbf{U}}=\begin{bmatrix}\mathbf{u}\\ \lambda\end{bmatrix},\quad \tilde{\mathbf{F}}=\begin{bmatrix}\mathbf{0}\\ \mathbf{q}\end{bmatrix}.\tag{C9}$$

[1] N. Gao and K. Lu, An underwater metamaterial for broadband acoustic absorption at low frequency, Appl. Acoust. **169**, 107500 (2020).
[2] N. Gao and Y. Zhang, A low frequency underwater metastructure composed by helix metal and viscoelastic damping rubber, J. Vib. Control **25**, 538 (2018).
[3] Y. Gu, H. Zhong, B. Bao, Q. Wang, and J. Wu, Experimental investigation of underwater locally multi-resonant metamaterials under high hydrostatic pressure for low frequency sound absorption, Appl. Acoust. **172**, 107605 (2021).
[4] L. E. Kinsler, A. R. Frey, and W. G. Mayer, Fundamentals of acoustics, Arch. Acoust. **16**, 56 (1963).
[5] A. Leblanc and A. Lavie, Three-dimensional-printed membrane-type acoustic metamaterial for low frequency sound attenuation, J. Acoust. Soc. Am. **141**, EL538 (2017).
[6] J. Mei, G. Ma, M. Yang, Z. Yang, W. Wen, and P. Sheng, Dark acoustic metamaterials as super absorbers for low-frequency sound, Nat. Commun. **3**, 756 (2012).
[7] A. N. Norris, Acoustic metafluids, J. Acoust. Soc. Am. **125**, 839 (2009).
[8] B. Yuan, Y. Chen, B. Tan, and B. Li, Statistical optimization of underwater lower-frequency sound insulation for locally resonant sonic material using genetic algorithm, Arch. Acoust. **44**, 365 (2019).
[9] Y. Chen, B. Zhao, X. Liu, and G. Hu, Highly anisotropic hexagonal lattice material for low frequency water sound insulation, Extreme. Mech. Lett. **40**, 100916 (2020).
[10] Y. Chen, M. Zheng, X. Liu, Y. Bi, Z. Sun, P. Xiang, J. Yang, and G. Hu, Broadband solid cloak for underwater acoustics, Phys. Rev. B **95**, 180104 (2017).
[11] X. Man, B. Xia, Z. Luo, J. Liu, K. Li, and Y. Nie, Engineering three-dimensional labyrinthine fractal acoustic metamaterials with low-frequency multi-band sound suppression, J. Acoust. Soc. Am. **149**, 308 (2021).
[12] J. P. Marage and Y. Mori, *Sonar and underwater acoustics* (Wiley, Hoboken, NJ, USA, 2013).
[13] C. J. Naify, T. P. Martin, C. N. Layman, M. Nicholas, A. L. Thangawng, D. C. Calvo, and G. J. Orris, Underwater acoustic omnidirectional absorber, Appl. Phys. Lett. **104**, 073505 (2014).
[14] Y. Tian, Q. Wei, Y. Cheng, Z. Xu, and X. Liu, Broadband manipulation of acoustic wavefronts by pentamode metasurface, Appl. Phys. Lett. **107**, 221906 (2015).
[15] H. Wu, C. Hao, and H. Zhang, Underwater broadband sound insulation with chiral spiral structures, AIP. Adv. **10**, 125022 (2020).
[16] Y. Xue and X. Zhang, Self-adaptive acoustic cloak enabled by soft mechanical metamaterials, Extreme. Mech. Lett. **46**, 101347 (2021).
[17] Y. Chen, X. Liu, P. Xing, and G. Hu, Pentamode material for underwater acoustic wave control, Adv. Mech. **46**, 201609 (2016).

[18] C. Cai, Z. Wang, Y. Chu, G. Liu, and Z. Xu, The phononic band gaps of bragg scattering and locally resonant pentamode metamaterials, J. Phys. D: Appl. Phys. **50**, 415100 (2017).

[19] Z. Liu, X. Zhang, Y. Mao, Y. Y. Zhu, Z. Yang, C. T. Chan, and P. Sheng, Locally resonant sonic materials, Science **289**, 1734 (2000).

[20] K. Yi and M. Collet, Broadening low-frequency bandgaps in locally resonant piezoelectric metamaterials by negative capacitance, J. Sound. Vib. **493**, 115837 (2021).

[21] K. Yu, N. X. Fang, G. Huang, and Q. Wang, Magnetoactive acoustic metamaterials, Adv. Mater. **30**, 1706348 (2018).

[22] H. Zhao, J. Wen, D. Yu, and X. Wen, Low-frequency acoustic absorption of localized resonances: Experiment and theory, J. Appl. Phys. **107**, 1734 (2010).

[23] T. Brunet, A. Merlin, B. Mascaro, K. Zimny, J. Leng, O. Poncelet, C. Aristegui, and O. Mondain-Monval, Soft 3D acoustic metamaterial with negative index, Nat. Mater. **14**, 384 (2015).

[24] Z. Huang, S. Zhao, M. Su, Q. Yang, Z. Li, Z. Cai, H. Zhao, X. Hu, H. Zhou, F. Li, *et al.*, Bioinspired patterned bubbles for broad and low-frequency acoustic blocking, ACS Appl. Mater. Interfaces **12**, 1757 (2020).

[25] M. S. Kushwaha, B. Djafari-Rouhani, and L. Dobrzynski, Sound isolation from cubic arrays of air bubbles in water, Phys. Lett. A **248**, 252 (1998).

[26] M. Minnaert, XVI, On musical air-bubbles and the sounds of running water, London, Edinburgh, Dublin. Philos. Mag. J. Sci. **16**, 235 (2009).

[27] Y. Bi, H. Jia, Z. Sun, Y. Yang, H. Zhao, and J. Yang, Experimental demonstration of three-dimensional broadband underwater acoustic carpet cloak, Appl. Phys. Lett. **112**, 223502 (2018).

[28] T. Buckmann, M. Thiel, M. Kadic, R. Schittny, and M. Wegener, An elasto-mechanical unfeelability cloak made of pentamode metamaterials, Nat. Commun. **5**, 4130 (2014).

[29] J. Christensen, M. Kadic, M. Wegener, O. Kraft, and M. Wegener, Vibrant times for mechanical metamaterials, MRS Commun. **5**, 453 (2015).

[30] S. H. Jo, Y. Xia, A. G. Moura, H. Yoon, Y. C. Shin, A. Erturk, and B. D. Youn, Experimentally validated broadband self-collimation of elastic waves, Int. J. Mech. Sci. **192**, 106131 (2021).

[31] M. Kadic, T. Bückmann, N. Stenger, M. Thiel, and M. Wegener, On the practicability of pentamode mechanical metamaterials, Appl. Phys. Lett. **100**, 191901 (2012).

[32] Y. Chen, X. Liu, and G. Hu, Influences of imperfectness and inner constraints on an acoustic cloak with unideal pentamode materials, J. Sound. Vib. **458**, 62 (2019).

[33] K. Wang, M. Cai, P. Zhou, and G. Hu, Homogenization in a simpler way: Analysis and optimization of periodic unit cells with Cauchy–Born hypothesis, Struct. Multidiscipl. Optim. **64**, 3911 (2021).